

Decoupling of optoelectronic properties from morphological changes in sodium treated kesterite thin film solar cells

C. Andres^{a,*}, T. Schwarz^b, S.G. Haass^a, T.P. Weiss^a, R. Carron^a, R. Caballero^c, R. Figi^d,
C. Schreiner^d, M. Bürki^d, A.N. Tiwari^a, Y.E. Romanyuk^a

^a Laboratory for Thin Films and Photovoltaics, Empa – Swiss Federal Laboratories for Materials Science and Technology, Ueberlandstrasse 129, 8600 Dübendorf, Switzerland

^b Department of Microstructure Physics and Alloy Design, Max-Planck-Institut für Eisenforschung GmbH, Max-Planck-Straße 1, 40237 Düsseldorf, Germany

^c Universidad Autónoma de Madrid, Departamento de Física Aplicada, C/ Francisco Tomás y Valiente 7, 28049 Madrid, Spain

^d Laboratory for Advanced Analytical Technologies, Empa – Swiss Federal Laboratories for Materials Science and Technology, Ueberlandstrasse 129, 8600 Dübendorf, Switzerland

ARTICLE INFO

Keywords:

Thin films solar cells
Kesterite
Rapid thermal processing
Sodium doping

ABSTRACT

Sodium is typically used during the synthesis of kesterite thin films to enhance the performance of solar cells. As sodium tends to affect grain growth and morphology, it is difficult to analyse solely the electronic effects of sodium as dopant. To decouple the structural and electronic effects from each other, two processes were designed in this work to successfully incorporate sodium into a vacuum-processed $\text{Cu}_2\text{ZnSnSe}_4$ absorber without changing the morphology. A thin layer of NaF is deposited before precursor deposition (Pre-NaF) or after absorber synthesis to undergo a post deposition treatment (NaF-PDT). While composition and distribution of matrix elements remain unchanged, the sodium concentration is increased upon sodium treatment up to 140 ppm as measured by inductively coupled plasma mass spectrometry. X-ray photoelectron spectroscopy showed that the surface composition was not altered. Within its detection limit, sodium was not present at the absorber surface. For a Pre-NaF sample measured with atom probe tomography a sodium concentration of 30 ppm was measured in a grain, suggesting that sodium might segregate at grain boundaries. The additional sodium content in the film leads to an increased acceptor concentration, which results in improved open-circuit voltage and fill factor.

1. Introduction

The addition of sodium with different procedures into kesterite thin films is widely used to increase the performance of the corresponding solar cells. Historically, sodium was introduced into absorber layers by out-diffusion from the soda-lime glass (SLG) substrate at elevated processing temperatures (Scheer and Schock, 2011a). To achieve a better control over the quantity of sodium in the absorber film several methods have been reported. Vacuum-based processes rely on sodium doped molybdenum back contacts (López-Marino et al., 2016) or an additional sodium containing layer (Lee et al., 2015; Li et al., 2013; Sutter-Fella et al., 2014; Gershon et al., 2015), while for solution-processing routes, a sodium salt can be directly dissolved into the precursor solution (Werner et al., 2015). If sodium is supplied before or during the synthesis of the kesterite thin film, a major impact on crystal growth and morphology is observed. The changes in morphology are often accompanied by changes in optical and electronic properties (Altamura

et al., 2013; Kim et al., 2014; Tampo et al., 2017). However, the observed effects are a superposition stemming from the changed morphology and the optoelectronic effect of sodium as a dopant. Only little work has been published (Rey et al., 2017), where sodium is introduced after the final absorber crystallization in a so-called post-deposition treatment (PDT), which is a quite well investigated topic for $\text{Cu}(\text{In,Ga})\text{Se}_2$ solar cells (Rudmann et al., 2005; Pianezzi et al., 2014; Reinhard et al., 2015).

In order to study solely the effect of sodium as a dopant, we designed two processes (Fig. 1) that allow the incorporation of low (< 0.1 at.%) quantities of sodium into the $\text{Cu}_2\text{ZnSnSe}_4$ (CZTSe) absorber without affecting the morphology. CZTSe absorbers are produced from a co-sputtered metal precursor with a thick selenium capping layer followed by rapid thermal processing (RTP), which leads to homogenous and reproducible $5 \times 5 \text{ cm}^2$ large solar cell devices. In a first approach, a thin sodium fluoride precursor layer is deposited on top of molybdenum (Pre-NaF). The second approach consists of a thin

* Corresponding author.

E-mail address: christian.andres@empa.ch (C. Andres).

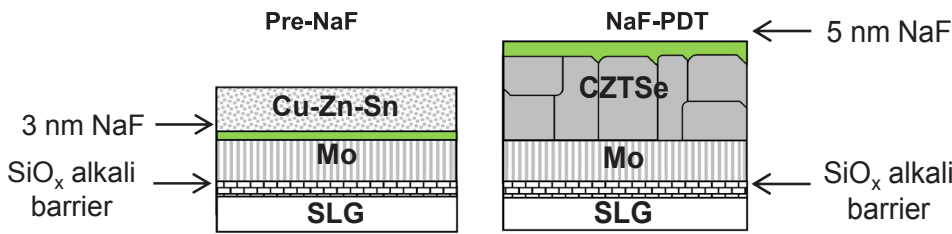


Fig. 1. Schematics of the two processes for sodium incorporation. *Left:* For the Pre-NaF process, a thin NaF layer is deposited on top of Molybdenum. *Right:* For the NaF-PDT, a thin NaF layer is deposited on the crystallized CZTSe absorber before undergoing a subsequent annealing in nitrogen atmosphere.

sodium fluoride layer deposited on the CZTSe absorber, which subsequently undergoes a heat treatment under nitrogen atmosphere (NaF-PDT). As a result, absorbers with similar morphology and composition but different electronic properties are obtained. Therefore, the effect of grain growth and morphology is decoupled from the intrinsic doping properties of sodium in CZTSe. The distribution of sodium on surface, bulk and grain boundaries is measured and the influences on defect energies, doping concentration and photovoltaic parameters are investigated.

2. Experimental details

The molybdenum back contact was deposited using DC sputtering on top of soda lime glass covered by an approx. 250 nm thick silicon oxide layer as the alkali diffusion barrier. A mixed Cu-Zn-Sn precursor was deposited by co-sputtering of elemental metal targets (Cu: 99.999%, 3.6 W/cm²; Zn: 99.995%, 2.9 W/cm²; Sn: 99.999%, 4.0 W/cm²) at room temperature in a con-focal arrangement (ATC-Orion 5 system from AJA Inc.). The precursor composition with Cu/(Zn + Sn) = 0.75 and Zn/Sn = 1.35 was deduced from the individual sputter rates and confirmed by energy-dispersive X-ray (EDX) measurements. A sputtering time of 12.5 min at an Ar base pressure of 0.26 Pa resulted in a precursor thickness of 400 nm. For all experiments, the same metal precursor recipe was used. Prior to the annealing, a 1.15 μ m thick selenium capping layer was thermally evaporated on top of the unheated metal precursor in order to reduce elemental losses and to enhance homogeneity during the annealing (Andres et al., 2017). The precursor was heated to 550 °C for 5 min with additional selenium pellets (800 mg) in a closed graphite reactor in a RTP system (AS-ONE 150 from Annealsys). The annealing was performed using a nitrogen base pressure of 62,500 Pa and a fast heating from room temperature to 550 °C at a rate of 4 °C/s and a natural cooling from 550 °C to 300 °C in 5 min. As-deposited CZTSe absorbers were subsequently covered with a CdS buffer by chemical bath deposition, followed by the deposition of the i-ZnO/ZnO:Al window by RF magnetron sputtering. In the final step a Ni/Al grid was deposited by e-beam evaporation and individual cells of 0.36 cm² designated area were mechanically scribed. No anti-reflection coating was used.

For the incorporation of sodium, a thermal evaporation system was used to deposit a thin sodium fluoride layer without substrate heating. In case of the Pre-NaF process, a 3 nm thin sodium fluoride layer was deposited on molybdenum prior to sputtering of metals. It has to be pointed out that for our process absorbers with thicker sodium fluoride layers as well as samples without alkali barrier suffered from strong blister formation after the selenization similar to Malerba et al. (2016). In the NaF-PDT process, a 5 nm thin sodium fluoride layer was deposited on top of the absorber and underwent a second heat treatment for 20 min at 300 °C at atmospheric N₂ base pressure without additional selenium. In contrast to Cu(In,Ga)Se₂ (Rudmann et al., 2005), a degradation took place when selenium was present during the annealing. It should be also mentioned, that an annealing without sodium fluoride layer lead to a strong deterioration of the devices, so that the changes in optoelectronic properties can be directly connected to the presence of the sodium fluoride layer.

The morphology was studied by scanning electron microscopy (SEM, HITACHI S-4800 at an acceleration of 5 kV and an emission

current of 10 μ A). Top-view images were taken from bare absorbers and cross-sections from complete solar cells. The bulk composition was determined from X-ray fluorescence (XRF) at an acceleration voltage of 45 kV. For inductively coupled plasma mass spectrometry (ICP-MS) analysis, kesterite absorber material was detached from the molybdenum back contact, directly transferred into 50 ml trace metal-free pre-cleaned polyethylene tubes and fully dissolved in a mixture of 2.5 ml H₂O₂ 30% MERCK suprapure, 4 ml HNO₃ 67% MERCK ultrapure and 2.5 ml HCl 32% MERCK ultrapure. After filling to 25 ml with 18 M Ω cm deionized water, the sample was diluted 1:10 with 18 M Ω cm deionized water for analysis. Element determinations were performed on an Agilent 8800 triple quadrupole ICP-MS with different reaction modes such as He and O₂ and external calibration using certified metal standards (1000 μ g ml⁻¹, Alfa Aesar Specpure). For quality assurance, analysis of reference materials and spiking experiments were performed, with recoveries between 90% and 110%. As a prerequisite the background contribution of sodium to the measurement was determined by opening an additional empty vial (blank) during the preparation of the analysis matter before following the same quantification procedure. An average from 5 blanks resulted in a sodium background signal of 180 ppm with respect to the in average collected absorber mass. The sodium background was subtracted from the measured sodium concentration. Depth profiling data from complete solar cells were obtained with a time-of-flight secondary ion mass spectrometry (ToF-SIMS) 5 system from ION-TOF. Bi⁺ ions were used as primary ions and positive ions were detected. Sputtering was performed using O₂⁺ sputtering ions with 2 keV ion energy, 400 nA ion current and a 300 \times 300 μ m² raster size. An area of 100 \times 100 μ m² was analyzed using Bi⁺ ions with 25 keV ion energy.

X-ray Photoelectron Spectroscopy (XPS) measurements were performed using a Quantum2000 from Physical Electronics with a monochromatic Al K α source (1486.6 eV). The work function of the instrument was calibrated on a regular basis to a binding energy of 83.95 eV (FWHM = 0.8 eV) for the Au 4f_{5/2} peak and the linearity of the energy scale is checked according to ISO 15472. Survey spectra were recorded with an energy step size of 0.5 eV and a pass energy of 117.40 eV. For depth profiling, detailed peak spectra were recorded with an energy step size of 0.2 eV and a pass energy of 46.95 eV (FWHM of Au 4f_{5/2} = 1.07 eV under the given conditions). An electron flood gun operated at 2.5 eV and an ion neutralizer using Ar⁺ of approx. 1 eV were used to minimize the fluctuations of the binding energy values due to sample charging. Spectra were recorded at a base pressure below 8 \times 10⁻⁹ mbar. A surface sputter depth profile was conducted by Ar⁺ sputtering at 0.5 keV for 60 s the first 5 min and for 300 s after 5 min before each acquisition.

The preparation of atom probe tomography (APT) specimens was carried out using a dual-beam focused-ion-beam (FIB, FEI Helios Nanolab 600i), according to the lift-out technique in Thompson et al. (2007). To minimize beam damage due to Ga implantation, a low energy Ga beam of 5 keV was used for final shaping of the APT specimens. Laser-assisted APT analyses were performed using a local electrode atom probe (LEAP™5000XS, Cameca Instruments). Laser pulses of 355 nm wavelength, \sim 10 ps pulse length, 200 kHz pulse frequency, and an energy of 5 pJ were applied at a base temperature of 50 K, and a detection rate of 10 ions per 1000 pulses was maintained constant. The J–V characterization was performed under the standard test conditions

(100 mW cm⁻², 25 °C, simulated AM1.5 Global spectrum) using a solar simulator calibrated with a certified Si diode. The external quantum efficiency (EQE) spectra were recorded using a chopped white light source (900 W halogen lamp) with a LOT MSH-300 monochromator, which was calibrated with certified Si and Ge diodes. The illuminated area on the sample was 0.1 cm² including grid lines. Admittance measurements were carried out with a LCR meter from Agilent (E4990A) with an AC voltage of 30 mV. Samples were kept overnight in the dark prior to the measurement to ensure a relaxed state. Capacitance-frequency (C-f) measurements for frequencies between 200 Hz and 2 MHz were performed at zero bias for a temperature range of 123–303 K. Activation energies of defects were obtained by simultaneously fitting the C-f spectra (Weiss et al., 2014). Capacitance-voltage (C-V) measurements were acquired for voltages between -1.0 V and 0.5 V at 1000 Hz for a temperature range of 123–323 K.

3. Results and discussion

3.1. Composition and morphology

As a prerequisite for this study, the processes were designed in a manner that composition and morphology were not altered upon the sodium treatment in order to reveal the doping effect on the optoelectronic properties. Table 1 presents the composition of the absorber as measured by XRF. All absorbers possessed typical Cu-poor (Cu/(Zn + Sn) < 1) and Zn-rich (Zn/Sn > 1) composition with small variations which are within the error of the XRF measurement. The NaF-PDT sample was measured before and after the post deposition treatment without exhibiting any compositional variation. The sodium fluoride layer was still present after the PDT and was removed after rinsing with deionized water. The majority of studies, which addressed Na-doping in CZTSe observed a strong change in morphology [3, 4]. In this work, we do not observe any change in morphology as shown in Fig. 2. The SEM top-view and cross-section images show for all samples a non-compact and rough morphology. The surface of all absorber layers is partially covered by the bright appearing ZnSe islands, which was observed for CZTSe layers grown with thick selenium capping layer (Andres et al., 2017).

3.2. Quantification of sodium

The 5 nm thick sodium fluoride layer on top of the 2 μm-thick absorber corresponds to the nominal sodium concentration of 1000 ppm, whereas an actual sodium concentration within the CZTSe layer is expected to be much lower due to the loss of sodium during annealing and CBD processing. To quantify the actual amount of sodium which is finally incorporated into the absorber films, ICP-MS measurements of each absorber were performed. The measured sodium concentration is given in Table 1. The reference sample with a sodium concentration of only 70 ppm shows quantitatively the effectiveness of the alkali barrier layer, taking into account that samples without barrier layer were reported with around 2000 ppm (Sutter-Fella, 2014). To prove the effectiveness qualitatively, devices were produced with our process on alkali free borosilicate glass and have shown similar solar cell efficiency as on soda-lime glass with SiO_x barrier (not shown here). The Na-

Table 1

Composition of the absorber as measured by XRF. Deviations are within the error of the measurement setup. Sodium concentration of the absorber as measured by ICP-MS.

	Cu/Zn	Cu/Sn	Cu/(Zn + Sn)	Zn/Sn	Na/ppm
Reference	1.38	1.71	0.76	1.24	70
NaF-PDT	1.38	1.68	0.76	1.22	110
Pre-NaF	1.35	1.72	0.76	1.27	140

treated samples in this work exhibit sodium concentrations 1.5–2.0 times higher than the reference, indicating an additional incorporation of sodium by both processes.

3.3. Surface analysis

To evaluate possible chemical modifications of the surface for the different sodium treatments, XPS has been performed. Fig. 3 shows the survey spectra of samples with different sodium treatments. In case of the NaF-PDT, the sample was rinsed with deionized water to remove residual sodium fluoride from the surface. While all matrix elements are clearly detectable with its core level and Auger peaks, Na cannot be detected in any of the samples. This agrees with the observations made in Gershon et al. (2015), where sodium could be only detected on the surface when the grain growth was enhanced. The matrix elements exhibit similar peak intensities for all samples. Therefore, no accumulation of sodium on the surface can be found within the detection limit of XPS and no change in surface composition can be observed. This finding coincides with the observations made for the NaF-PDT in Cu(In,Ga)Se₂ (Reinhard et al., 2015). A distinct oxygen peak is visible in the survey but was eliminated after the first sputtering step during profiling. Unfortunately, traces of iodine were found due to mask contamination from other iodine containing samples. XPS depth profiles of the samples are presented in Fig. 4 using the core level intensities of Cu 3p_{3/2}, Zn 2p_{3/2}, Sn 3d_{5/2} and Se 3d_{5/2}. All samples show a Sn-enrichment towards the surface, which is eliminated during the first sputtering step. The overall surface composition is not affected by the sodium treatments. As a result, the changes in photovoltaic parameters cannot be explained due to surface modifications.

3.4. Distribution of sodium

The distribution of sodium along the depth of the absorber was analyzed by TOF-SIMS as presented in Fig. 5. Qualitatively, the total number of counts for sodium throughout the whole depth is higher in case of the sodium treated samples, indicating the incorporation of sodium into the film. While the reference sample shows a flat distribution within the absorber and a distinct increase at the back contact, the sodium treated samples exhibit a steady increase towards the back contact. Interestingly, the NaF-PDT sample has a lower Na signal at the absorber surface as compared to the Pre-NaF sample. This might stem from the additional rinsing with deionized water before the CBD, which typically wash out the sodium from the surface. In contrast to the reference sample and the Pre-NaF sample, where sodium seems to accumulate to a higher extent at the back, the NaF-PDT sample has a more even distribution. As the Pre-NaF sample exhibits a lower sodium signal in the bulk region compared to the NaF-PDT sample in TOF-SIMS but a higher sodium concentration in ICP-MS, it can be assumed that in case of the Pre-NaF sample the major part of sodium is located at the interfaces.

Na tends to segregate along the grain boundary (GB) in kesterite absorbers rather than be incorporated inside the grain bulk as has been measured by atomic probe tomography (APT) (Schwarz et al., 2013, 2015) and transmission electron microscopy (TEM) (Thersleff et al., 2017). In order to assess how much Na is incorporated inside the grains, we performed complimentary APT measurements on one Pre-NaF sample. The sodium concentration was found to be ~30 ppm (~0.003 at.% or 1.3 · 10¹⁷ cm⁻³) in the grain interior, which is on the same order as the value of 0.006 at.% reported for co-evaporated CZTSe absorbers with sodium out-diffusing from SLG substrates (Schwarz et al., 2015). Taking into account that the Na concentration obtained from the ICP-MS is 140 ppm (Table 2) accounting for grain boundaries and grain interiors, it can be concluded that a major part of Na should indeed be located along the GB. It has to be pointed out however, that the kesterite material can exhibit several types of grain boundaries and the concentration of sodium is different at various GBs (Schwarz et al.,

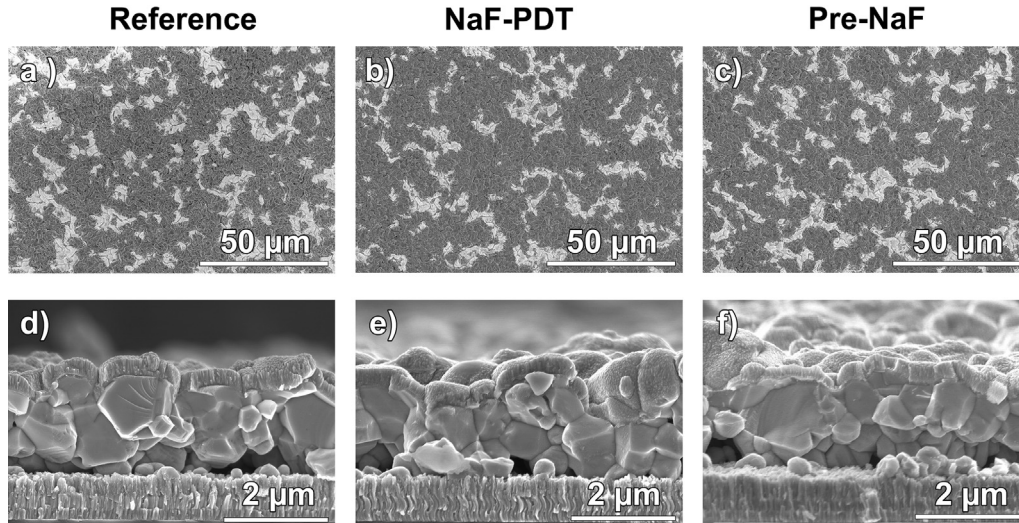


Fig. 2. SEM top-view images of (a) Reference, (b) NaF-PDT, (c) Pre-NaF absorbers and SEM cross-sections of (d) Reference, (e) NaF-PDT, (f) Pre-NaF cells.

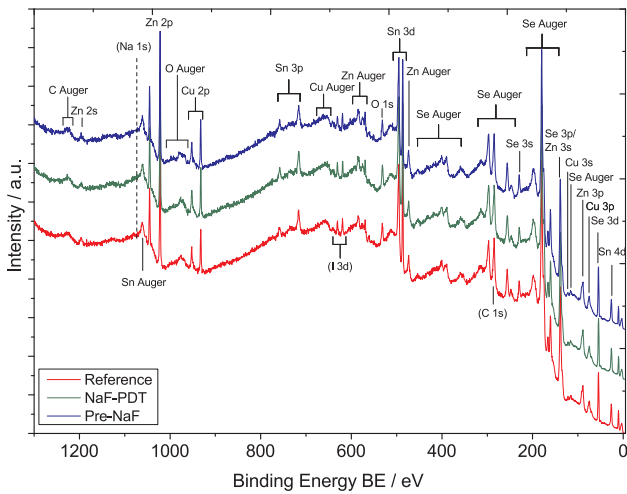


Fig. 3. XPS survey spectra of samples with different sodium treatments. While the Reference and the Pre-NaF sample were measured as deposited, the NaF-PDT sample was washed with DI water to remove residual NaF from the surface. For none of the samples sodium could be detected within the detection limit of XPS. Iodine was present due to contamination of the sample holder masks.

2015; Thersleff et al., 2017). One example of such “irregular” grain boundary measured by APT can be found in SI, Fig. S1, where the sodium concentration inside a Zn-enriched region is lower than that inside the CZTSe grain. This type of GBs has already been observed in Schwarz et al. (2015) where nanometer-sized ZnSe grains could be detected at or near GBs.

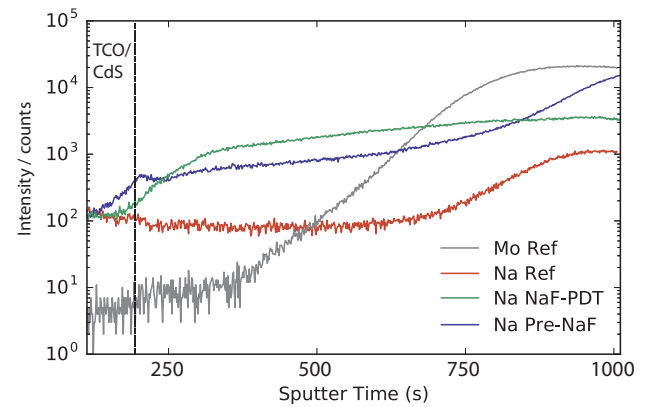


Fig. 5. SIMS depth profiles of solar cells with different sodium treatment. For each sample, the sputtering time was aligned to the molybdenum signal (Mo Ref) to cancel out fluctuations in sputter rates.

Table 2

Summary of defects extracted by fitting of the C-f-measurements. In contrast to the sodium treated samples, no shallow defect could be observed in the reference sample. The exact values depend on the quality of the capacitance fits and can vary by several meV.

	E_A (Defect 1)/meV	E_A (Defect 2)/meV	E_A (Defect 3)/meV
Reference	n/a	155	385
NaF-PDT	28	115	374
Pre-NaF	82	146	290

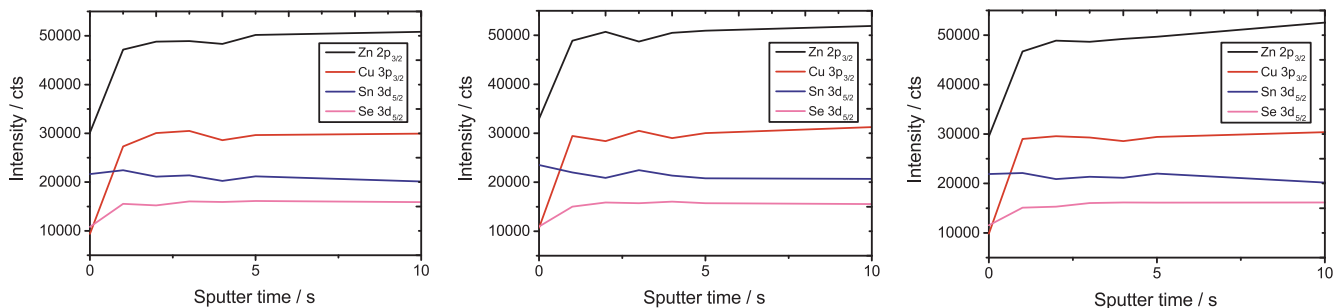


Fig. 4. XPS depth profiles of matrix elements for *left*: Reference, *center*: NaF-PDT and *right*: Pre-NaF. No significant differences can be observed for the different samples.

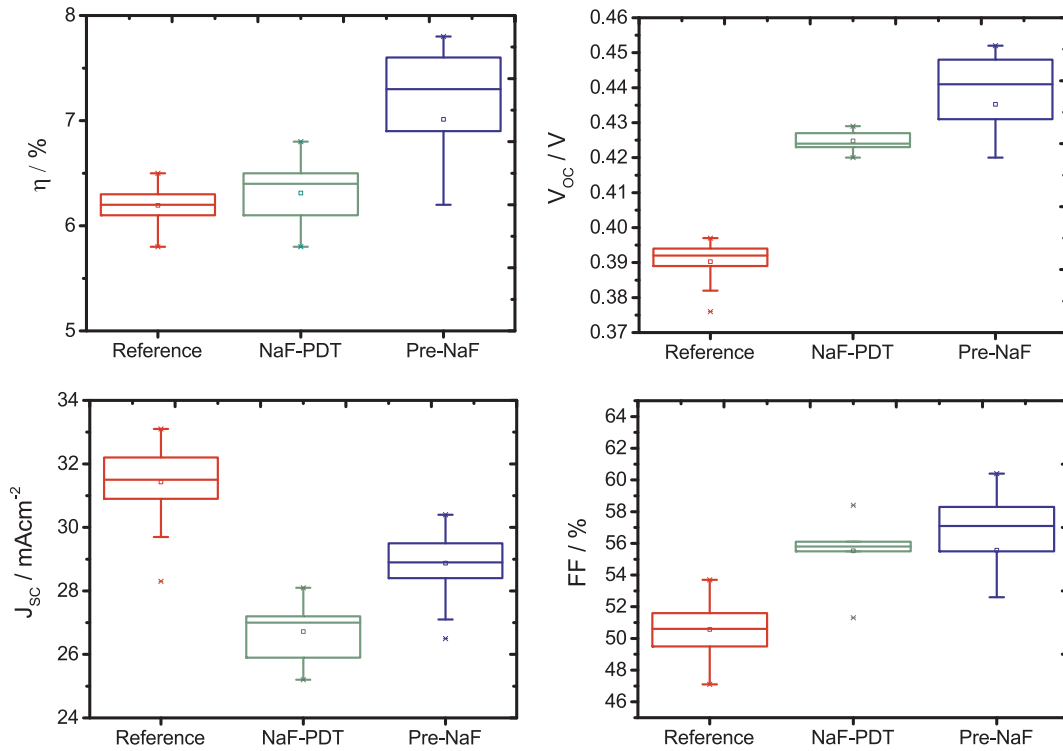


Fig. 6. Efficiency (η), open-circuit voltage (V_{OC}), short-circuit current density (J_{SC}) and fill factor (FF) of solar cells with different sodium treatment. The graphs represent highest, average and median values obtained from 49 solar cells of 0.36 cm^2 area located on $5 \times 5 \text{ cm}^2$ substrates.

3.5. Solar cell parameters

In accordance with previous studies (Li et al., 2013; Abzieher et al., 2016; Sutter-Fella et al., 2014), sodium incorporation into CZTSe thin film solar cells increases the open-circuit voltage and fill factor. Fig. 6 compares efficiency (η), open-circuit voltage (V_{OC}), short-circuit current density (J_{SC}) and fill factor (FF) of the different devices. An increase in V_{OC} by 30 mV for the NaF-PDT sample and by 50 mV for the Pre-NaF can be observed. The FF follows a similar trend, resulting in absolute increase of 5% for the NaF-PDT sample and 7% for the Pre-NaF sample. The improvement in FF is correlated with an improvement in series and shunt resistances. Both sodium treated samples suffer from a loss in J_{SC} by 2–4 mA/cm², being most prominent for the NaF-PDT sample. EQE measurements (Fig. 7) reveal that the loss in current density occurs in the whole wavelength region but is more pronounced towards longer wavelengths. The latter finding indicates a deteriorated carrier collection, which might stem from a lower lifetime/diffusion length of minority carriers and/or a reduced space charge region (SCR) width. The

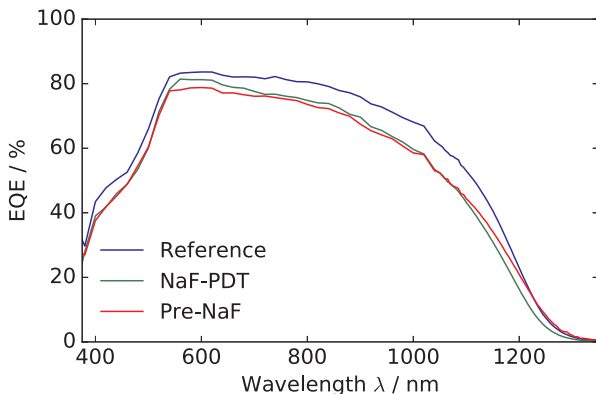


Fig. 7. External Quantum Efficiency measurements of samples with different sodium treatment.

reason for the loss in EQE for all wavelengths remains unclear as we could not find a direct evidence for the existence of a current blocking barrier (Scheer and Schock, 2011b). The bandgap calculated from the inflection point is around 1.03–1.04 eV for all samples. Hence, the increase in V_{OC} is not related to a bandgap shift. Consequently, the overall absolute efficiency gain for the NaF-PDT and the Pre-NaF sample is 0.5% and 1.5%, respectively, as compared to nominally Na-free reference.

3.6. Influence of sodium doping on admittance spectra

In order to reveal the effect of sodium as an electrical dopant, C-V and C-f measurements were performed. From C-V measurements, Mott-Schottky plots are derived in order to calculate the apparent doping concentration $N_{CV,min}$ (Fig. 8). For each sample a temperature near the SCR capacitance was selected in order to reduce the contributions of deep defects (Weiss et al., 2016). Upon sodium incorporation, the apparent doping concentration increases from $2.2 \cdot 10^{15} \text{ cm}^{-3}$ to $7.3 \cdot 10^{15} \text{ cm}^{-3}$ for the NaF-PDT and to $1.1 \cdot 10^{16} \text{ cm}^{-3}$ for the Pre-NaF. The sodium concentration in the grain interior is about one magnitude higher in case of the Pre-NaF, which suggests that not every sodium atom acts as an acceptor (e.g. Na_{Cu} is considered to be neutral-charge (Maeda et al., 2015)). For the estimation of the open-circuit voltage increase due to increased acceptor concentration, the following formula is used (Pianezzi et al., 2014):

$$\Delta V_{OC} = \frac{k_B T}{q} \log \left(\frac{N_{CV,NaF}}{N_{CV,Ref}} \right)$$

Being k_B Boltzmann's constant, T the room temperature, q the elementary charge, $N_{CV,Ref}$ the apparent doping density of the Reference sample and $N_{CV,NaF}$ the respective sodium treated sample. A V_{OC} increase of 30 mV for the NaF-PDT and a 40 mV increase for the Pre-NaF can be calculated, which is in good agreement with the results from JV measurements. In this case, the relative change in apparent doping density seems to correlate with the actual acceptor concentration. A

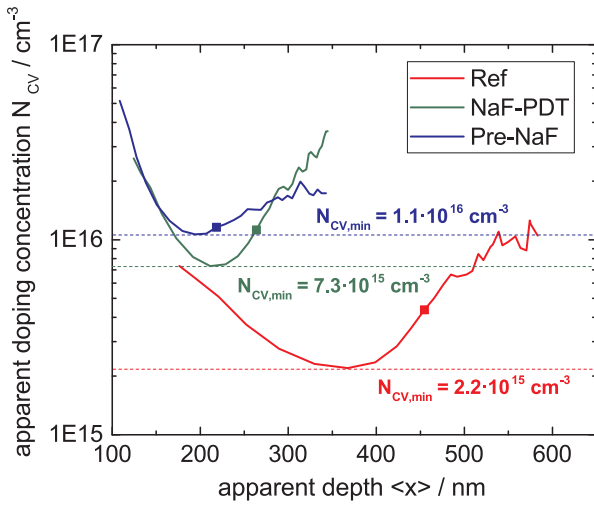


Fig. 8. Derivative of Mott-Schottky plot of samples with different sodium treatment deduced from C-V-measurements taken at 1000 Hz. $N_{CV,min}$ represents minimum value of the apparent doping concentration curve. The solid square points correspond to the measurement at zero bias and allow a comparison of the space charge region width.

higher doping concentration is generally causing a decrease in SCR width. Assuming a constant minority carrier lifetime/diffusion length, the reduced SCR would explain the loss in current density which is observed in the EQE for longer wavelengths in the case of the sodium treated samples.

Fig. 9 presents the C-f spectra for the different samples. The geometrical capacitance (solid grey lines in **Fig. 9**) and the space charge region capacitance (dashed lines in **Fig. 9**) are calculated via

$$C_{geo} = \frac{\epsilon_r \epsilon_0}{d}$$

and

$$C_{SCR} = \sqrt{\frac{\epsilon_r \epsilon_0 q N_{CV}}{2V_{bi}}}$$

respectively, with the relative permittivity $\epsilon_r = 8.6$ (Persson, 2010), the vacuum permittivity ϵ_0 , an absorber thickness $d = 2 \mu\text{m}$, the elementary charge q , the apparent doping concentration $N_{CV,min}$ and a built-in voltage of 500 mV (determined from Mott-Schottky plots in forward bias). The reference sample exhibits a shallow defect below the space charge region capacitance line (Defect 2) and a deep defect above (Defect 3). The deep defect can also be observed for the sodium treated samples. While the shallow defect in the reference sample shows a symmetric behavior in the derivative of the capacitance spectra (**Fig. S2**), the sodium treated samples possess a pronounced shoulder, which indicates the existence of an additional defect. A deconvolution of the two shallow defects is done by simultaneously fitting the C-f spectra

(Weiss et al., 2014) to extract the activation energy of the additional shallow defect (Defect 1). The calculated defect energies are summarized in **Table 2**. Defect 2 is present in all samples with an activation energy of $130 \pm 20 \text{ meV}$ and is reported with similar energy in Barkhouse et al. (2012), Brammertz et al. (2013), Li et al. (2013), and Weiss et al. (2016). The deep defect 3 is located at around $345 \pm 45 \text{ meV}$. Deep defects with similar or higher activation energies were also observed in Li et al. (2013) and Weiss et al. (2016). The sodium treated samples exhibit an additional shallow defect around $50 \pm 30 \text{ meV}$, which is in good agreement with the data from literature (Li et al., 2013; Rey et al., 2017). The results suggest that the additional shallow defect which is observed for the sodium treated sample is responsible for the increase in apparent doping concentration.

4. Conclusion

We investigated two different processes for sodium incorporation without altering the composition and morphology to allow a systematic study of the doping effect of sodium onto electronic properties of CZTSe layers. In a first approach, the Pre-NaF process uses a thin sodium fluoride layer on molybdenum before metal precursor deposition to allow sodium doping during the selenization process. In a second approach, the doping with sodium is realized with a post-deposition treatment (NaF-PDT) of the as-synthesized absorber. Using ICP-MS, we could show for both processes that a few tens of ppm increase in the sodium concentration is sufficient to have a beneficial effect on optoelectronic properties. XPS measurements could neither detect sodium on the surface of the absorber nor any compositional changes in the near-surface region. Chemical or morphological surface modifications are therefore not visible and they are not responsible for changes in the electronic properties of CZTSe layers. From SIMS depth profiling, Na-treated samples exhibited an increased sodium signal towards the molybdenum back contact, suggesting a preferred location at the Mo/CZTSe interface. APT measurements reveal that the sodium concentration in the grain interior is only 30 ppm, while 140 ppm were measured in the absorber film by ICP-MS, which indicates that sodium is primarily segregated at the grain boundaries. Interestingly, sodium was not detected for a grain boundary, which presented a Zn enriched composition. Therefore, sodium seems to accumulate preferably at grain boundaries where the composition of matrix elements is unchanged (Schwarz et al., 2015). Sodium is responsible for the appearance of an additional shallow defect and the enhanced acceptor concentration as measured by admittance spectroscopy. The higher acceptor concentration improves η , V_{OC} and FF but decreases the near-infrared response in the EQE due to a lower SCR width.

Acknowledgements

Financial support from the Swiss National Science Foundation (SNF) in the network of the Indo-Swiss Joint Research Programme (ISJRP) [IZLIZ2_157140/1] is gratefully acknowledged. The authors would like

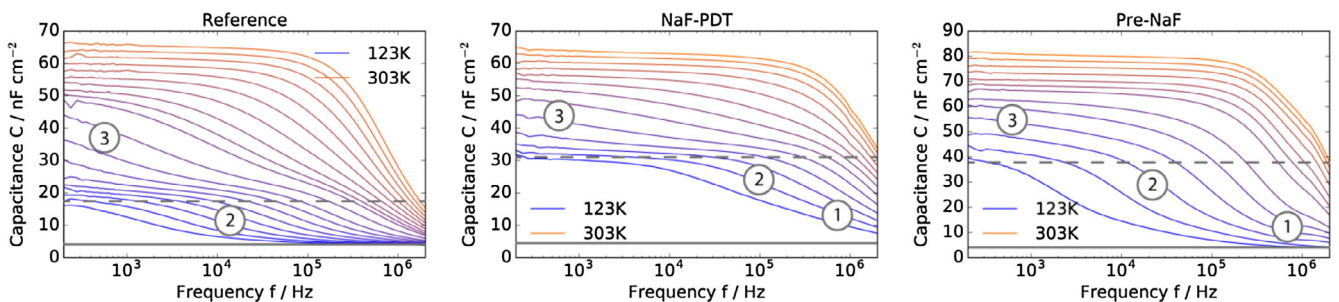


Fig. 9. C-f-measurements in the temperature interval 123–303 K for samples with different sodium treatments at zero bias. Geometrical capacitance is marked as a solid line, space charge region capacitance as a dashed line. The numbered circles represent the corresponding defects.

to thank the whole team of the Laboratory for Thin Films and Photovoltaics and Uwe Tezins and Andreas Sturm for their support to the APT, SEM and FIB facilities at Max-Planck-Institut für Eisenforschung GmbH. T. Schwarz is grateful for the support of the German Research Foundation (DFG) [Contract GA 2450/1-1]. R. Caballero acknowledges financial support from Spanish MINECO within the Ramón y Cajal program [RYC-2011-08521], MINECO project WINCOST [ENE2016-80788-C5-2-R] and from Spanish Ministry of Education, Culture and Sport within the José Castillejo program [CAS 15/00070].

Appendix A. Supplementary material

Supplementary data associated with this article can be found, in the online version, at <http://dx.doi.org/10.1016/j.solener.2018.03.067>.

References

- Abzieher, T., Schnabel, T., Hetterich, M., Powalla, M., Ahlswede, E., 2016. Source and effects of sodium in solution-processed kesterite solar cells. *Phys. Status Solidi A* 213, 1039–1049. <http://dx.doi.org/10.1002/pssa.201532619>.
- Altamura, G., Roger, C., Grenet, L., Bleuse, J., Fournier, H., Perraud, S., Mariette, H., 2013. Influence of sodium-containing substrates on Kesterite CZTSSe thin films based solar cells. *MRS Online Proc. Libr. Arch.* 1538, 103–106. <http://dx.doi.org/10.1557/opl.2013.1000>.
- Andres, C., Haass, S.G., Romanyuk, Y.E., Tiwari, A.N., 2017. 9.4% efficient $\text{Cu}_2\text{ZnSnSe}_4$ solar cells from co-sputtered elemental metal precursor and rapid thermal annealing. *Thin Solid Films* 633, 141–145. <http://dx.doi.org/10.1016/j.tsf.2016.09.048>. (E-MRS 2016 Spring Meeting, Symposium V, Thin-Film Chalcogenide Photovoltaic Materials).
- Barkhouse, D.A.R., Gunawan, O., Gokmen, T., Todorov, T.K., Mitzi, D.B., 2012. Device characteristics of a 10.1% hydrazine-processed $\text{Cu}_2\text{ZnSn}(\text{Se},\text{S})_4$ solar cell. *Prog. Photovolt. Res. Appl.* 20, 6–11. <http://dx.doi.org/10.1002/ppp.1160>.
- Brammertz, G., Buffière, M., Oueslati, S., ElAnzeery, H., Ben Messaoud, K., Sahayaraj, S., Köble, C., Meuris, M., Poortmans, J., 2013. Characterization of defects in 9.7% efficient $\text{Cu}_2\text{ZnSnSe}_4$ -CdS-ZnO solar cells. *Appl. Phys. Lett.* 103, 163904. <http://dx.doi.org/10.1063/1.4826448>.
- Gershon, T., Shin, B., Bojarczuk, N., Hopstaken, M., Mitzi, D.B., Guha, S., 2015. The role of sodium as a surfactant and suppressor of non-radiative recombination at internal surfaces in $\text{Cu}_2\text{ZnSnS}_4$. *Adv. Energy Mater.* 5, 1400849. <http://dx.doi.org/10.1002/aenm.201400849>.
- Kim, G.Y., Kim, J., Jo, W., Son, D.-H., Kim, D.-H., Kang, J.-K., 2014. Nanoscale investigation of surface potential distribution of $\text{Cu}_2\text{ZnSn}(\text{S},\text{Se})_4$ thin films grown with additional NaF layers. *Nano Converg.* 1, 1–8.
- Lee, Y.S., Gershon, T., Gunawan, O., Todorov, T.K., Gokmen, T., Virgus, Y., Guha, S., 2015. $\text{Cu}_2\text{ZnSnSe}_4$ thin-film solar cells by thermal co-evaporation with 11.6% efficiency and improved minority carrier diffusion length. *Adv. Energy Mater.* 5, 1401372. <http://dx.doi.org/10.1002/aenm.201401372>.
- Li, J.V., Kuciauskas, D., Young, M.R., Repins, I.L., 2013. Effects of sodium incorporation in co-evaporated $\text{Cu}_2\text{ZnSnSe}_4$ thin-film solar cells. *Appl. Phys. Lett.* 102, 163905. <http://dx.doi.org/10.1063/1.4802972>.
- López-Marino, S., Sánchez, Y., Espindola-Rodríguez, M., Alcóbé, X., Xie, H., Neuschitzer, M., Becerril, I., Giraldo, S., Dimitrievska, M., Placidi, M., Fourdrinier, L., Izquierdo-Roca, V., Pérez-Rodríguez, A., Saucedo, E., 2016. Alkali doping strategies for flexible and light-weight $\text{Cu}_2\text{ZnSnSe}_4$ solar cells. *J. Mater. Chem. A* 4, 1895–1907. <http://dx.doi.org/10.1039/C5TA09640E>.
- Maeda, T., Kawabata, A., Wada, T., 2015. First-principles study on alkali-metal effect of Li, Na, and K in $\text{Cu}_2\text{ZnSnS}_4$ and $\text{Cu}_2\text{ZnSnSe}_4$. *Phys. Status Solidi C* 12, 631–637. <http://dx.doi.org/10.1002/pssc.201400345>.
- Malerba, C., Valentini, M., Azanza Ricardo, C.L., Rinaldi, A., Cappelletto, E., Scardi, P., Mittiga, A., 2016. Blistering in $\text{Cu}_2\text{ZnSnS}_4$ thin films: correlation with residual stresses. *Mater. Des.* 108, 725–735. <http://dx.doi.org/10.1016/j.matdes.2016.07.019>.
- Persson, C., 2010. Electronic and optical properties of $\text{Cu}_2\text{ZnSnS}_4$ and $\text{Cu}_2\text{ZnSnSe}_4$. *J. Appl. Phys.* 107, 053710. <http://dx.doi.org/10.1063/1.3318468>.
- Pianezzi, F., Reinhard, P., Chirilă, A., Bissig, B., Nishiwaki, S., Buecheler, S., Tiwari, A.N., 2014. Unveiling the effects of post-deposition treatment with different alkaline elements on the electronic properties of CIGS thin film solar cells. *Phys. Chem. Chem. Phys.* 16, 8843–8851. <http://dx.doi.org/10.1039/C4CP00614C>.
- Reinhard, P., Bissig, B., Pianezzi, F., Avancini, E., Hagendorfer, H., Keller, D., Fuchs, P., Döbeli, M., Vigo, C., Crivelli, P., Nishiwaki, S., Buecheler, S., Tiwari, A.N., 2015. Features of KF and NaF postdeposition treatments of $\text{Cu}(\text{In,Ga})\text{Se}_2$ absorbers for high efficiency thin film solar cells. *Chem. Mater.* 27, 5755–5764. <http://dx.doi.org/10.1021/acs.chemmater.5b02335>.
- Rey, G., Babbe, F., Weiss, T.P., Elanzeery, H., Melchiorre, M., Valle, N., Adib, B.E., Siebentritt, S., 2017. Post-deposition treatment of $\text{Cu}_2\text{ZnSnSe}_4$ with alkalis. *Thin Solid Films* 633, 162–165. <http://dx.doi.org/10.1016/j.tsf.2016.11.021>. (E-MRS 2016 Spring Meeting, Symposium V, Thin-Film Chalcogenide Photovoltaic Materials).
- Rudmann, D., Brémaud, D., Zogg, H., Tiwari, A.N., 2005. Na incorporation into $\text{Cu}(\text{In,Ga})\text{Se}_2$ for high-efficiency flexible solar cells on polymer foils. *J. Appl. Phys.* 97, 084903. <http://dx.doi.org/10.1063/1.1857059>.
- Scheer, R., Schock, H.-W., 2011a. Thin film technology. In: *Chalcogenide Photovoltaics*. Wiley-VCH Verlag GmbH & Co. KGaA, pp. 235–275. <http://dx.doi.org/10.1002/9783527633708.ch5>.
- Scheer, R., Schock, H.-W., 2011b. Appendix A: frequently observed anomalies. In: *Chalcogenide Photovoltaics*. Wiley-VCH Verlag GmbH & Co. KGaA, pp. 305–314. <http://dx.doi.org/10.1002/9783527633708.ch7>.
- Schwarz, T., Cojocaru-Mirédin, O., Choi, P., Mousel, M., Redinger, A., Siebentritt, S., Raabe, D., 2013. Atom probe study of $\text{Cu}_2\text{ZnSnSe}_4$ thin-films prepared by co-evaporation and post-deposition annealing. *Appl. Phys. Lett.* 102, 042101. <http://dx.doi.org/10.1063/1.4788815>.
- Schwarz, T., Cojocaru-Mirédin, O., Choi, P., Mousel, M., Redinger, A., Siebentritt, S., Raabe, D., 2015. Atom probe tomography study of internal interfaces in $\text{Cu}_2\text{ZnSnSe}_4$ thin-films. *J. Appl. Phys.* 118, 095302. <http://dx.doi.org/10.1063/1.4929874>.
- Sutter-Fella, C.M., 2014. *Solution-processed Kesterite Absorbers for thin Film Solar Cells*. [Ph.D. Thesis]. ETH Zurich.
- Sutter-Fella, C.M., Stükelberger, J.A., Hagendorfer, H., La Mattina, F., Kranz, L., Nishiwaki, S., Uhl, A.R., Romanyuk, Y.E., Tiwari, A.N., 2014. Sodium assisted sintering of chalcogenides and its application to solution processed $\text{Cu}_2\text{ZnSn}(\text{S},\text{Se})_4$ thin film solar cells. *Chem. Mater.* 26, 1420–1425. <http://dx.doi.org/10.1021/cm403504u>.
- Tampo, H., Kim, K.M., Kim, S., Shibata, H., Niki, S., 2017. Improvement of minority carrier lifetime and conversion efficiency by Na incorporation in $\text{Cu}_2\text{ZnSnSe}_4$ solar cells. *J. Appl. Phys.* 122, 023106. <http://dx.doi.org/10.1063/1.4993288>.
- Thersleff, T., Giraldo, S., Neuschitzer, M., Pistor, P., Saucedo, E., Leifer, K., 2017. Chemically and morphologically distinct grain boundaries in Ge-doped $\text{Cu}_2\text{ZnSnSe}_4$ solar cells revealed with STEM-EELS. *Mater. Des.* 122, 102–109. <http://dx.doi.org/10.1016/j.matdes.2017.02.077>.
- Thompson, K., Lawrence, D., Larson, D.J., Olson, J.D., Kelly, T.F., Gorman, B., 2007. In situ site-specific specimen preparation for atom probe tomography. *Ultramicroscopy* 107, 131–139. <http://dx.doi.org/10.1016/j.ultramic.2006.06.008>.
- Weiss, T.P., Redinger, A., Regesch, D., Mousel, M., Siebentritt, S., 2014. Direct evaluation of defect distributions from admittance spectroscopy. *IEEE J. Photovolt.* 4, 1665–1670. <http://dx.doi.org/10.1109/JPHOTOV.2014.2358073>.
- Weiss, T.P., Redinger, A., Rey, G., Schwarz, T., Spies, M., Cojocaru-Mirédin, O., Choi, P., Siebentritt, S., 2016. Impact of annealing on electrical properties of $\text{Cu}_2\text{ZnSnSe}_4$ absorber layers. *J. Appl. Phys.* 120, 045703. <http://dx.doi.org/10.1063/1.4959611>.
- Werner, M., Sutter-Fella, C.M., Hagendorfer, H., Romanyuk, Y.E., Tiwari, A.N., 2015. $\text{Cu}_2\text{ZnSn}(\text{S},\text{Se})_4$ solar cell absorbers processed from Na-containing solutions in DMSO. *Phys. Status Solidi A* 212, 116–120. <http://dx.doi.org/10.1002/pssa.201431146>.